OPEN ACCESS

Original research

CAF-macrophage crosstalk in tumour microenvironments governs the response to immune checkpoint blockade in gastric cancer peritoneal metastases

Yuanfang Li ,[1] Yongqiang Zheng ,[1] Jiaqian Huang,[1] Run-Cong Nie ,[1] Qi-Nian Wu,[1] Zhijun Zuo,[1] Shuqiang Yuan ,[1] Kai Yu,[1] Cheng-Cai Liang,[1] Yi-Qian Pan,[1] Bai-Wei Zhao,[1] Yuhong Xu,[1] Qihua Zhang,[1] Yashang Zheng,[1] Junquan Chen,[1] Zhao-Lei Zeng,[1] Wei Wei,[1] Ze-Xian Liu ,[1] Rui-Hua Xu ,[1,2] Hui-Yan Luo[1]

► Additional supplemental material is published online only. To view, please visit the journal online (https://doi.org/10.1136/gutjnl-2024-333617).

[1]State Key Laboratory of Oncology in South China, Collaborative Innovation Center for Cancer Medicine, Guangdong Provincial Clinical Research Center for Cancer, Sun Yat-sen University Cancer Center, Guangzhou, Guangdong, China
[2]Research Unit of Precision Diagnosis and Treatment for Gastrointestinal Cancer, Chinese Academy of Medical Sciences, Guangzhou, Guangdong, China

Correspondence to
Dr Hui-Yan Luo; luohy@sysucc.org.cnProfessor Rui-Hua Xu; xurh@sysucc.org.cn and Dr Ze-Xian Liu; liuzx@sysucc.org.cn

YL, YZ, JH, R-CN, Q-NW and ZZ are joint first authors.

Received 14 August 2024
Accepted 23 October 2024

To cite: Li Y, Zheng Y, Huang J, *et al*. *Gut* Epub ahead of print: [*please include* Day Month Year]. doi:10.1136/gutjnl-2024-333617

ABSTRACT

Background Peritoneal metastasis is the most common metastasis pattern of gastric cancer. Patients with gastric cancer peritoneal metastasis (GCPM) have a poor prognosis and respond poorly to conventional treatments. Recently, immune checkpoint blockade (ICB) has demonstrated favourable efficacy in the treatment of GCPM. Stratification of best responders and elucidation of resistance mechanisms of ICB therapies are highly important and remain major clinical challenges.

Design We performed a phase II trial involving patients with GCPM treated with ICB (sintilimab) combined with chemotherapy. The samples of primary tumours, GCPMs and peripheral blood from patients were collected for single-cell sequencing to comprehensively interpret the tumour microenvironment of GCPM and its impacts on immunotherapy efficacy.

Results The GCPM ecosystem coordinates a unique immunosuppressive pattern distinct from that of primary GC, which is dominated by a stroma-myeloid niche composed of SPP1+tumour-associated macrophages (TAMs) and Thrombospondin 2 (THBS2)+matrix cancer-associated fibroblasts (mCAFs). Consequently, this stroma-myeloid crosstalk is the major mediator of ICB resistance in patients with GCPM. Mechanistically, the accumulated THBS2+mCAFs facilitate the recruitment of peritoneum-specific tissue-resident macrophages and their transformation into SPP1+TAMs via the complement C3 and its receptor C3a receptor 1 (C3AR1), thereby forming a protumoral stroma-myeloid niche. Blocking the C3-C3AR1 axis disrupts the stroma-myeloid crosstalk and thereby significantly improves the benefits of ICB in *in vivo* models.

Conclusion Our findings provide a new molecular portrait of cell compositions associated with ICB resistance in patients with GCPM and aid in the prioritisation of therapeutic candidates to potentiate immunotherapy.

WHAT IS ALREADY KNOWN ON THIS TOPIC

⇒ The most recent evidence from two phase III randomised trials yielded positive results indicating that patients with gastric cancer peritoneal metastases (GCPM) benefit significantly from immune checkpoint blockade (ICB) treatments.

⇒ Stratification of patients who benefit most from ICB therapies and elucidation of the mechanisms of ICB resistance are highly important and remain major clinical challenges.

INTRODUCTION

Gastric cancer (GC) remains a major global health problem, especially in East Asian countries.[1–4] A common site of GC metastasis is the peritoneal cavity (peritoneal metastasis (GCPM)), with up to 55%–60% of patients with GC developing peritoneal metastases.[5] Peritoneal metastasis is life-threatening for patients with GC, and patients with GCPM are often highly symptomatic, with the 5-year overall survival (OS) rate decreasing to only 2%.[6–8] Systemic chemotherapy is the standard-of-care treatment for recurrent or metastatic GC, but it often fails in patients with GCPM. When peritoneal metastases are present, patients receiving palliative systemic chemotherapy often survive <6 months.[9 10]

Immune checkpoint blockade (ICB) has revolutionised the treatment of GC, but previous studies have shown that patients with GCPM have limited and transient benefits from ICB therapies.[11–13] Fortunately, the most recent evidence from two phase III randomised trials challenged the literature and yielded positive results indicating that patients with GC benefit significantly from ICB treatments regardless of whether peritoneal metastases are present.[14 15] Compared with chemotherapy alone, the CheckMate-649 trial revealed that first-line nivolumab plus chemotherapy reduces the mortality risk for patients with GCPM by approximately 30%.[14] Similarly, the RATIONALE-305 trial reported a significantly favourable outcome in patients with GCPM treated with first-line

WHAT THIS STUDY ADDS

⇒ Our research efforts have resulted in the establishment of the pioneering single-cell atlas of GCPM, which vividly delineates the unique ecosystem of GCPM, starkly contrasting that of primary GC and prominently featuring an enrichment of macrophages and stromal components.
⇒ Our analysis identified KLRD1+natural killer T cells as the major facilitator for the effectiveness of ICB treatment, which significantly expand in ICB-responsive tumours and possess extraordinary tumour-killing activity.
⇒ A stroma-myeloid niche composited of SPP1+tumour-associated macrophages and THBS2+matrix cancer-associated fibroblasts (mCAFs) terms to be the major mediator of ICB resistance in GCPM.
⇒ Most intriguingly, we made a novel discovery of a stroma-myeloid crosstalk via the C3-C3AR1 axis, which was found to promote tumour progression and ICB resistance.
⇒ Furthermore, blocking this axis disrupted the stroma-myeloid crosstalk, leading to a significant improvement in the efficacy of ICB in *in vivo* models and providing a new target for reversing immunotherapy resistance.

HOW THIS STUDY MIGHT AFFECT RESEARCH, PRACTICE OR POLICY

⇒ Our findings provide new insights into factors associated with ICB resistance in patients with GCPM.
⇒ Our findings would aid in the prioritisation of therapeutic candidates to potentiate immunotherapy.

tislelizuma plus chemotherapy, with an HR of 0.80.[15] Above all, ICB therapies shed new light on the management of GCPMs. Therefore, stratifying patients who would benefit most from ICB therapies and developing new approaches to facilitate ICB efficiency are highly important and remain major clinical challenges.

Therefore, we conducted a phase II clinical study to evaluate the efficacy and safety of the combination of immunotherapy and chemotherapy in the treatment of patients with GCPM. Then, a single-cell map encompassing >410 000 cells across five tissue types was established from patients enrolled in our clinical study to comprehensively characterise the tumour microenvironments (TME) and intratumoral heterogeneity of the GCPMs and address the cellular and molecular mechanisms related to immunotherapy efficiency. To our knowledge, this is the first study to investigate the molecular mechanisms of the ICB response of GCPMs at single-cell resolution.

RESULTS

A single-cell RNA sequencing atlas revealed the tissue-specific patterns of the TME in GCPM

The cohorts were derived from a phase II study with patients with GCPM treated with injectable paclitaxel (albumin-binding) via intraperitoneal perfusion combined with intravenous sindilimab, S-1 and oxaliplatin (GC-IP001 study; https://www.chictr.org.cn/showproj.html?proj=191640). Single-cell RNA sequencing (scRNA-seq) was performed on 21 surgical resection and biopsy GCPM samples, 7 primary GC samples, 5 peritumoral gastric normal (GN) samples, 1 peritoneal normal sample and 4 peripheral blood mononuclear cell (PBMC) samples (figure 1A and online supplemental table S1). As shown in online supplemental table S1, the samples were derived from 19 patients with GC, with 14 cases treated with ICB therapy, of which 5 patients exhibited partial response (PR) after treatment, 4 patients exhibited stable disease and 5 patients exhibited progressive disease (PD). Four patients treated with ICB had paired samples of GN, GC, GCPM and PBMC, and one patient treated with ICB had paired samples of GC and GCPM. The obtained scRNA-seq data were combined with a previously published scRNA-seq GC atlas,[16] along with three additional cases of GCPM (online supplemental table S2).

After rigorous quality control and filtering, we obtained 410 612 qualified single-cell transcriptomes across five tissue types including 24 GCPM and 31 GC samples (figure 1A,B). To define the major population and subpopulation structure of the TME, we performed graph-based clustering, which identified 16 subsets of TME cells, including B/plasma cells, T cells, natural killer (NK) cells, natural killer T (NKT) cells, dendritic cells (DCs), monocytes, neutrophils, macrophages, mast cells, cancer-associated fibroblasts (CAFs), pericytes (PCs) and endothelial cells (figure 1B,C and online supplemental figure S1A).

We performed tissue distribution analysis[17] and observed the predominance of mast cells and plasma cells in the GC/GN samples and the relative predominance of macrophages, endothelial cells and CAFs in the GCPM samples. Monocytes and neutrophils were enriched in the normal peritoneum samples, whereas NK cells, NKT cells and monocytes were enriched in the PBMC samples (figure 1D–F). Furthermore, Kyoto Encyclopedia of Genes and Genomes (KEGG) pathway analysis revealed that pathways related to the extracellular matrix and the complement and coagulation system were upregulated in GCPM, whereas inflammatory pathways were downregulated (figure 1G), indicating an inhibited immune response, extensive stromal components and enhanced angiogenesis in the GCPM samples (online supplemental figure S1B).

These compositional changes in GCPM were further verified via an in-house bulk RNA-seq cohort with 12 pairs of matched GN, GC and GCPM samples (online supplemental figure S2). M2 macrophages significantly infiltrated GCPMs (CIBERSORTx: p=0.001; XCell: p=0.0005) (online supplemental figure S2A–D). In addition, a significant increase of stromal components in GCPM samples was also verified, such as endothelial cells (p=0.02), mesenchymal stem cells (p=0.009) and preadipocytes (p=0.003) (online supplemental figure S2C,D).

We then subclustered the epithelial components (online supplemental figure S1C), and applied InferCNV[18] to infer the copy number variation (online supplemental figure S1D). Compared with those in the primary GC samples, the tumour cells in the GCPM samples presented greater intertumoral heterogeneity and lower intratumoral heterogeneity (online supplemental figure S1E–H).

Together, our results suggest that GCPM has a unique TME distinct from that of primary GC, presenting with a stroma-myeloid niche predominantly enriched in macrophages and stromal cells.

The transcriptional diversity of lymphocytes links NKT cells to the immunotherapy response in patients with GCPM

Unsupervised clustering analyses were performed on 72 774 CD4+ T cells, 90 374 cytotoxic lymphocytes (CTL) and 58 111 B/plasma cells (figure 2A–C). On the basis of the differentially expressed genes and canonical immune markers (online supplemental figure S3A–C), we defined five transcriptional states of CD4+ T cells: naïve-like (Tn, C1), central memory (Tcm, C2), follicular helper (C3), cytotoxic (C4) and regulatory (C5) CD4+ T cells. We defined five transcriptional states of CD8+ T cells: naïve-like (Tn, C1), central memory (Tcm, C2), effector memory

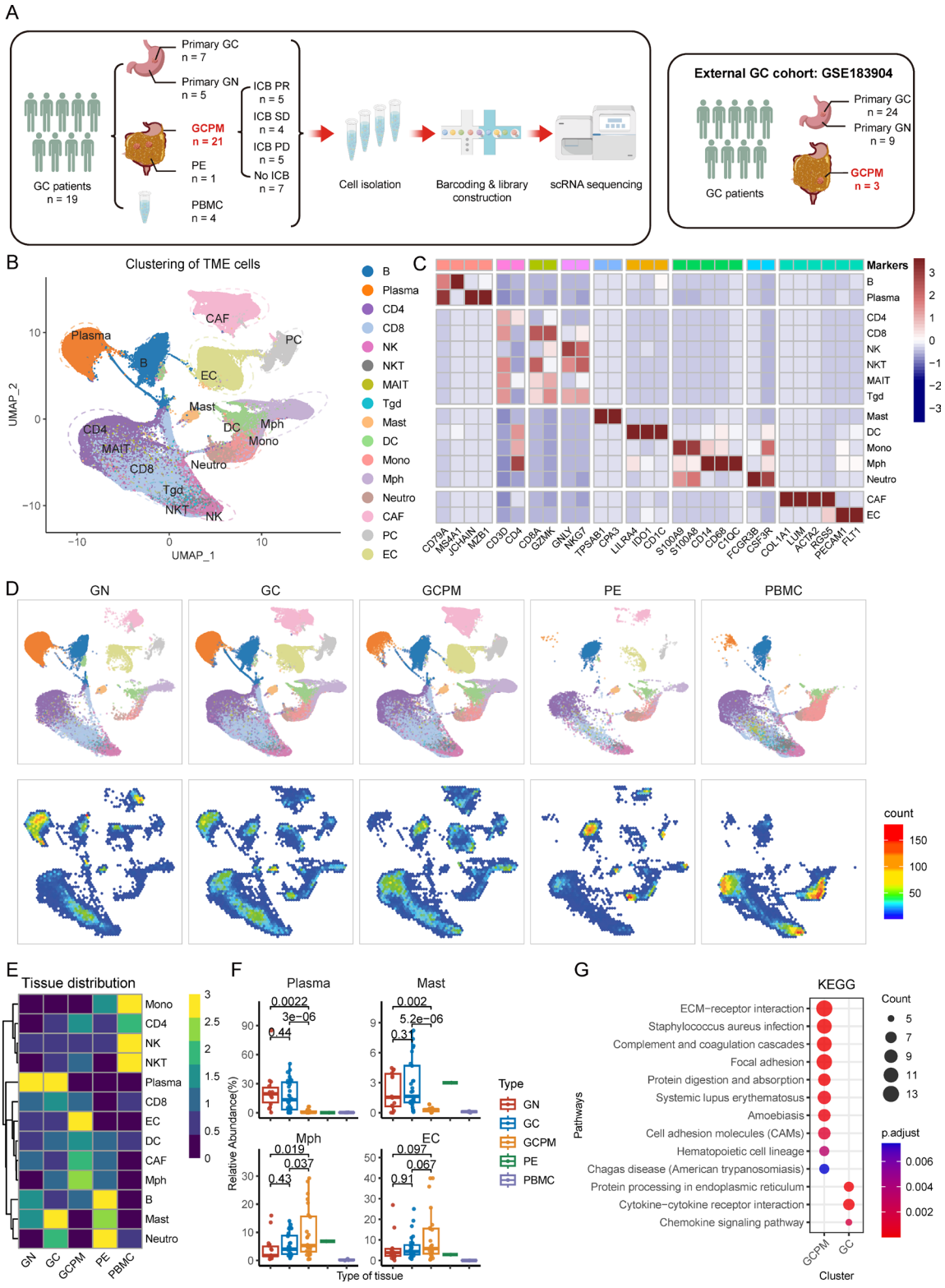

Figure 1 Study design and single-cell transcriptional atlas of peritoneal metastases of gastric cancer (GC). (A) Overview of the study design. (B) Uniform Manifold Approximation and Projection (UMAP) embedding of single-cell RNA sequencing (scRNA-seq) data for all 410 612 cells. (C) Heatmap showing the RNA expression of marker genes used to define the 15 major cell types. (D) UMAP embedding and cell abundance of scRNA-seq data for gastric normal (GN) tissues, primary GC tissues, gastric cancer peritoneal metastases (GCPM) tissues, peritoneal (PE) tissues and peripheral blood mononuclear cell (PBMC). (E) Heatmap displaying the distribution of 16 cell types across different tissue types (GN, GC, GCPM, PE and PBMC), as estimated by Ro/e. (F) Box plot comparing the abundances of plasma cells, mast cells, macrophages and endothelial cells across different tissue types, including GN (n=14), GC (n=31), GCPM (n=24), PE (n=1) and PBMC (n=4). The statistical significance was tested via Student's t-test. (G) Dot plot showing the results of Kyoto Encyclopedia of Genes and Genomes (KEGG) analyses of the differentially expressed genes between the GCPM and GC groups. CAF, cancer-associated fibroblasts; DC, dendritic cell; EC, endothelial cell; ICB, immune checkpoint blockade; NK, natural killer cell; NKT, natural killer T cell; PC, pericyte.

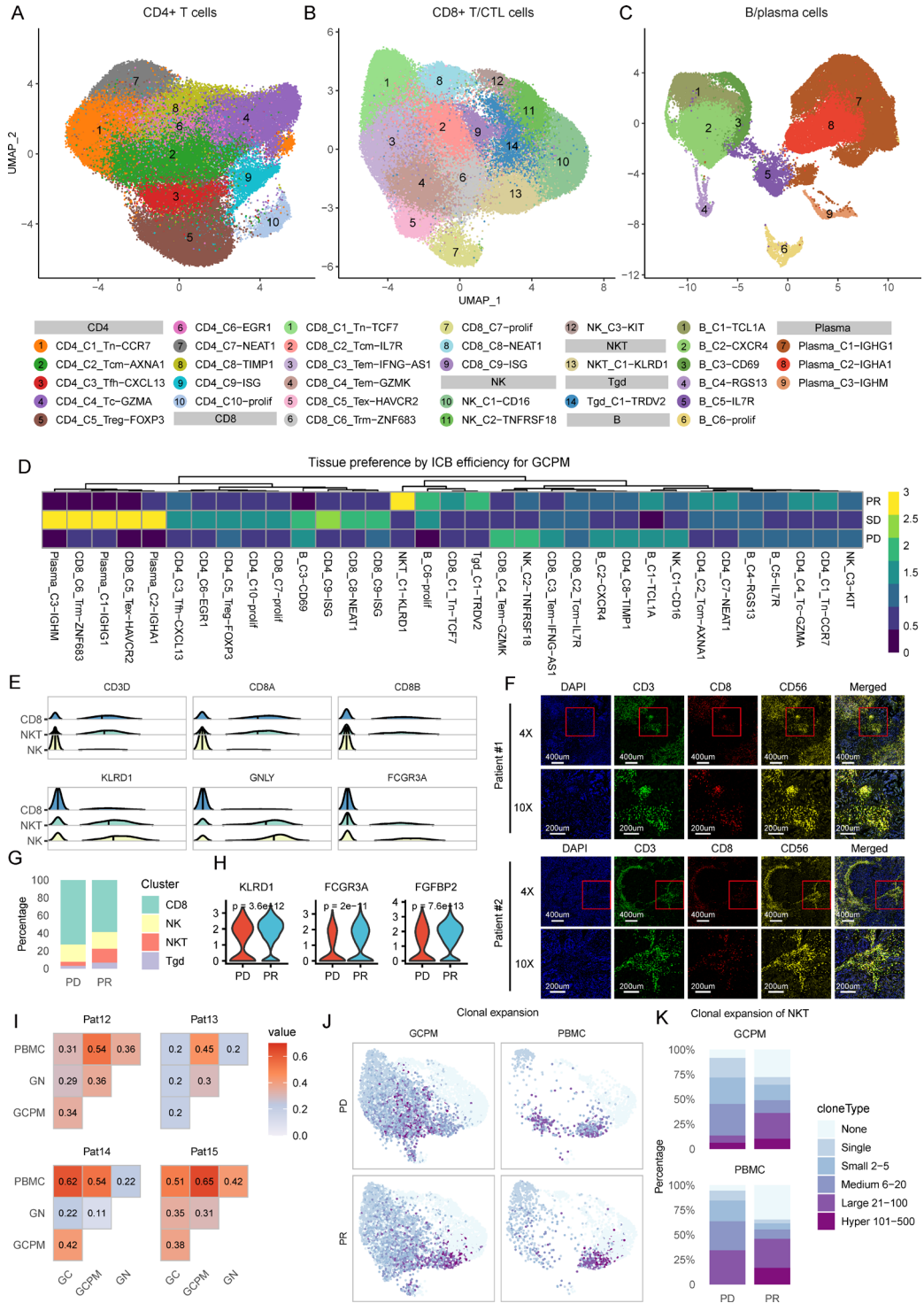

Figure 2 Lymphocyte landscape. (A) Uniform Manifold Approximation and Projection (UMAP) embedding of 10 CD4+ T-cell subclusters. (B) UMAP embedding of 14 cytotoxic lymphocyte (CTL) subclusters (9 CD8+ T-cell subclusters, 3 natural killer (NK) cell subclusters, 1 natural killer T (NKT) cell subcluster and 1 Tgd (γδT) cell subcluster). (C) UMAP embedding of nine B/plasma cell subclusters. (D) Heatmap displaying the distribution of lymphocytes across different immunotherapy responses, including partial response (PR), stable disease (SD) and progressive disease (PD), as estimated by Ro/e. (E) Ridgeline plot displaying the key markers used to define KLRD1+NKT cells, including T-cell markers (*CD3D*, *CD8A* and *CD8B*) and NK markers (*GNLY*, *KLRD1* and *FCGR3A*). (F) Multiplex immunofluorescence of DAPI, CD3, CD8 and CD56 in the gastric cancer peritoneal metastases (GCPM). The upper and the lower panels are images of two representative patients. (G) Stack plot displaying the abundance of CTL cells in response to immunotherapy (PR vs PD). (H) Violin plot comparing the expression of killer-like markers (*KLRD1* and *FGFBP2*) and killer receptors (*FCGR3A*) in KLRD1+NKT cells in response to immunotherapy (PR vs PD). The statistical significance was tested via Wilcoxon test. (I) Overlap of T-cell receptors of KLRD1+NKT cells across matched gastric normal (GN) tissues, primary gastric cancer (GC) tissues, GCPM tissues and peripheral blood mononuclear cell (PBMC) samples from patients treated with immunotherapy (n=4). (J) UMAP plot comparing the clonal expansion of CTLs in the GCPM and PBMC samples between PR patients and patients with PD. (K) Stack plot comparing the clonal expansion of CTLs in the GCPM and PBMC samples between PR patients and patients with PD. ICB, immune checkpoint blockade.

(C3-C4), exhausted (Tex, C5) and tissue-resident memory (C6) (figure 2A,B). In addition, we identified three types of innate cytotoxic lymphocytes, including γδT cells, NK cells and NKT cells (figure 2B). For B/plasma cells, we identified six clusters of B cells and three clusters of plasma cells (figure 2C). We further performed tissue distribution analysis,[17] which revealed preferential infiltration of HAVCR2+CD8+ Tex and IGHG+ plasma cells in GC, whereas the GCPM samples exhibited superior infiltration of NEAT1+CD4+ T cells, CXCR4+ B cells and TIMP1+CD4+ T cells (online supplemental figure S3D,E).

We conducted tissue distribution analysis according to the ICB response in GCPM,[17] and found that KLRD1+NKT cells were preferentially enriched in PR patients (figures 2D,G and online supplemental S3D). KLRD1+NKT cells exhibit both T-cell and NK-cell phenotypes,[19] with high expression of T-cell markers (such as *CD3D*, *CD8A* and *CD8B*) and NK-cell markers (such as *KLRD1*, *GNLY* and *CD16*) (figure 2E and online supplemental figure S3F). We performed multiplex immunofluorescence (mIF) assays to validate the phenotypes of NKT cells, and the colocalisation of CD3, CD8 and CD56 confirmed the high abundance of NKT cells in GCPM (figure 2F). We found that genes related to antigen recognition (ie, CD16) and cytotoxic functions (ie, *KLRD1* and *FGFBP2*) were highly expressed by NKT cells in PR patients (figure 2G,H and online supplemental figure S3G,H).

T-cell receptor (TCR) analyses revealed that CTL cells, especially NKT cells, exhibited greater clonal expansion (online supplemental figure S4A–F). We observed that CD4+ T cells shared few TCR clones across diverse subclusters, whereas CTL cells shared substantial numbers of TCR clones across diverse subclusters (online supplemental figure S4G,H). Intriguingly, NKT cells in GCPM had considerable overlap (45%–65%) with those from PBMCs (figure 2I and online supplemental figure S4I,J). Then, we extracted the GCPM-specific CTLs according to the method reported by Huang *et al*[20] and analysed the distribution of CTLs across diverse tissues, and the results revealed that there was a high abundance of GCPM-specific NKT cells in PBMC (online supplemental figure S4K,L). Thus, NKT cells might be the predominant tumour-killing cells in GCPM. In PR patients, NKT cells were extensively expanded in both GCPM and PBMCs (figure 2J,K) to a much greater extent than they were in patients with an unfavourable ICB response, establishing the relationships between the expansion of GCPM-specific NKT cells and the ICB response.

Overall, these data suggest that KLRD1+NKT cells are among the dominant cells involved in the ICB response of patients with GCPM. KLRD1+NKT cells might be a promising source of CAR-NKT-cell therapy.

The single-cell trajectory of myeloid cells illustrates that TRMs are the major source of TAMs in GCPM

We subclustered 55 981 myeloid cells and obtained 13 subsets according to the RNA expression of canonical markers (figure 3A,B and online supplemental figure S5A–C). Four DC subsets (C1–C4), plasmacytoid DCs (pDCs), cDC2s and cDC1s, were characterised by high expression of major histocompatibility complex class II molecules and low expression of CD14 (online supplemental figure S5A). Neutrophils were distinguished according to the expression of *FCGR3B* and *CSF3R*. The remaining clusters were identified as monocytes/Fmacrophages on the basis of their high expression of *CD14*, *CD68*, *CD163* and *MRC1*. Clusters expressing resident-like markers, including *F13A1*, *MRC1* and *FOLR2*,[21] were denoted as tissue-resident macrophages (TRMs; C2). Clusters expressing *CXCL9*, *MMP12* and *CXCL10* were defined as antitumour macrophages[22] (C3), whereas clusters expressing *TREM2*[23] and *SPP1*[24] were marked as TAMs (C4 and C5) (figure 3B and online supplemental figure S5A–B). Interestingly, SPP1+TAMs (C5) expressed high levels of *CD276*, *LGALS9* and *HAVCR2* (encoding T cell immunoglobulin and mucin domain 3 (TIM-3)) (online supplemental figure S5A–C), revealing its protumoral and immunosuppressive effects.[24 25] The differential abundance analysis identified compositional enrichment of neutrophils in primary GC, enrichment of monocytes in PBMCs and enrichment of TAMs in GCPM (figure 3C).

To explore the origin of the aberrantly infiltrated TAMs in GCPM, we used Monocle3[26] to construct single-cell trajectories of monocytes/macrophages. Interestingly, the Monocle3 algorithm yielded two independent developmental trajectories for monocytes/macrophages: (1) the first trajectory (branch 1) was monocyte-derived macrophages, with FCN1+monocytes found at earlier developmental timepoints and IL1B+monocytes and RETN+macrophages found at later developmental timepoints and (2) the second trajectory (branch 2) corresponded to TRM-derived TAMs, mapping F13A1+TRMs at the initial timepoint and SPP1+TAMs and CXCL9+macrophages at later developmental timepoints (figure 3D–F and online supplemental figure S5D–G).

Our results indicated that most TAMs in the GCPM population were TRM-derived (>60%), which is consistent with previous reports.[27] Therefore, we performed further analyses focused on TRM-derived macrophages to investigate their developmental trajectories (figure 3G–I and online supplemental figure S6). Intriguingly, pseudotime analysis revealed that the majority of F13A1+TRMs were positioned in a prebranch state, validating F13A1+TRMs as a major origin of macrophages, whereas CXCL9+macrophages and TAMs bifurcated into two independent cell fates after the branch point (figure 3G–I and online supplemental figure S6A). Interestingly, F13A1+TRM cells can develop into both antitumoral CXCL9+macrophages[22] and protumoral SPP1+TAMs,[28] whose polarity has been reported to form a network of cellular programmes that control human cancers.[22] In primary GN and GC tissues, F13A1+TRMs frequently differentiate into CXCL9+macrophages. In GCPM, differentiation into TAMs was markedly increased (figure 3I and online supplemental figure S6B–D).

To explore the factors driving these developmental alterations, we investigated the dynamic variations in transcription factors (TFs) among the different lineages. We found that both the TF activity and the expression levels of MAF (encoding MAF BZIP transcription factor) and TCF4 (encoding transcription factor 4) were greatest in F13A1+TRMs and decreased dramatically during the transition process. During the development of CXCL9+macrophages, we discovered significant upregulation of TF activity and the expression of IRF8 (encoding interferon regulatory factor 8), HIC1 (encoding HIC ZBTB transcriptional repressor 1) and NFATC1 (encoding nuclear factor of activated T cells 1). In the other developmental lineages of TAMs, TFs such as MLX (encoding MAX dimerisation protein MLX), CEBPA (encoding CCAAT enhancer binding protein alpha and ETS variant transcription factor 5) were overexpressed and dynamically activated (figure 3J–L and online supplemental figure S6E,F). We then verified the alterations in the activity of key TFs by exploring the expression of their regulons (online supplemental figure S6G–J).

Overall, we systematically deciphered the landscape and developmental trajectories of monocytes/macrophages in GCPM. We discovered a cluster of peritoneal cavity-enriched TRMs that can

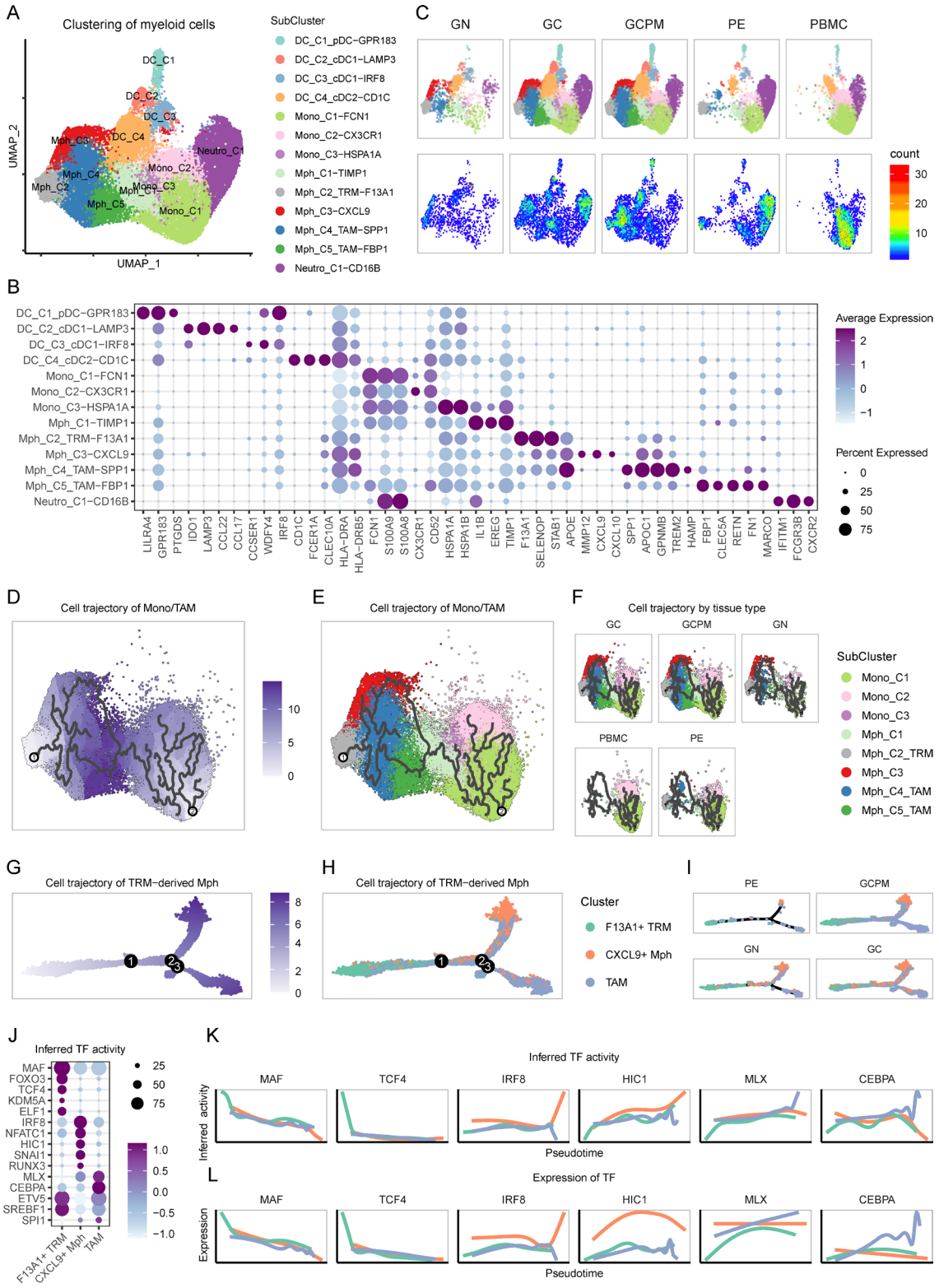

Figure 3 Landscape and cell trajectory of myeloid cells. (A) Uniform Manifold Approximation and Projection (UMAP) embedding of 13 myeloid cell subclusters (4 dendritic cell (DC) subclusters, 1 neutrophil subcluster, 3 monocyte subclusters and 5 macrophage subclusters). (B) Dot plot showing the RNA expression of marker genes used to define the myeloid cell types. (C) UMAP embedding and cell abundance of myeloid cells for gastric normal (GN) tissues, primary gastric cancer (GC) tissues and gastric cancer peritoneal metastases (GCPM) tissues and peritoneum (PE) tissues. (D) Pseudotime and (E) cell trajectories of monocytes/macrophages inferred by Monocle3. Two independent cell trajectories were identified: branch 1 represented monocyte-derived macrophages, and branch 2 represented macrophages derived from tissue-resident macrophages (TRMs). (F) Cell trajectories of monocytes/macrophages inferred by Monocle3 in five tissue types. (G) Pseudotime and (H) cell trajectories of TRM-derived macrophages inferred by Monocle2. (I) Cell trajectories of TRM-derived macrophages inferred by Monocle2 in the GN, GC, PE and GCPM groups. (J) Differential transcription factor (TF) activity between F13A1+TRM cells, CXCL9+macrophages and SPP1+tumour-associated macrophages (TAMs). (K) Dynamic changes in TF activity over time. (L) Dynamic change in corresponding TF expression over time.

develop into both SPP1+TAMs and CXCL9+macrophages. In GCPM, dynamic TF alterations are associated with the remodelling of the differential balance between SPP1+TAMs and CXCL9+macrophages.

SPP1+TAMs were associated with immunotherapy resistance in GCPM

Differential testing confirmed the significant trend of macrophage infiltration in GCPM, especially F13A1+TRMs (p=0.005) and SPP1+TAMs (p=0.056) (figure 4A). LAMP3+cDC1s were enriched in primary GC, and GPR183+pDCs were enriched in GCPM (figure 4A). LAMP3+cDC1s, which express high levels of PDL1 and PDL2 (online supplemental figure S5A), as well as exhausted CD8+ T cells, are central participants in tumour immunosuppression and are targets of ICB treatments.[17 28] The disparities between the aggressiveness of GCPM and the relatively low numbers of LAMP3+cDC1s (figure 4A) and exhausted CD8+ T cells (figure 2F) imply that distinct intrinsic mechanisms mediate immunosuppression in GCPM. Accordingly, we discovered that macrophages in GCPM presented increased levels of immunosuppressive markers, including *SPP1*, *TGFB1*, *TREM2* and *HAVCR2* (figure 4B). We then performed mIF assays to validate the abundance of TAMs between the GCPM and GC samples (marked by CD68 and TREM2) and observed significantly greater infiltration of TAMs in GCPM than in primary GC (figure 4C).

Among macrophages, SPP1+TAMs were linked to an impaired ICB response (PD) (figure 4D,E). Among the macrophages in GCPM, *SPP1*, *GPNMB, CD9* and *TREM2* were overexpressed in the ICB-resistant macrophages (figure 4F,G). A remarkable overexpression of *SPP1* was observed in ICB-resistant macrophages (figure 4G,H). Therefore, the myeloid niche composed of SPP1+TAMs in GCPM exhibited an immunosuppressive phenotype, which was linked with ICB resistance. Specifically, cell-cell communication analyses revealed that the SPP1-CD44 interaction between TAMs and CTLs was also significantly upregulated in the ICB-resistant group (figure 4I,J). The mIF assays of SPP1 and CD8/CD56 indicated that the area with high SPP1 expression presented relatively low CD8+ T cell and NK cell levels (figure 4K,L), confirming the exclusion effects of SPP1 on CTL cells.[29] These findings indicate that the infiltration of SPP1+TAMs into the GCPM niches was associated with immune escape and ICB resistance in GCPM.

Transcriptional diversity of stromal cells pinpointed THBS2+mCAFs as tumour promoters in GCPM

We then subclustered 58 570 stromal cells (figure 5A,B and online supplemental figure S7A–E). Two clusters of PCs, namely, mature PCs and immature PCs, were identified according to the high expression levels of *MYH9*/*MYH11* and *RGS5*/*THY1*[30] and the low expression level of *FAP*. The remaining clusters were identified as CAFs (defined by *FAP*), corresponding to matrix CAFs (mCAFs) defined by *ACTA2* (encoding αSMA) and *COL1A1*, and inflammatory CAFs (iCAFs) defined by inflammatory factors such as *CXCL1*, *CXCL14* and *CCL11* (figure 5A–C and online supplemental figure S6A). Further analyses suggested that THBS2+mCAFs expressed high levels of *IGF1* and *THBS2* (figure 5C and online supplemental figure S7A–E), both of which act as protumoral factors.[31 32]

The further differential abundance analysis via Milo[33] identified 6602 neighbourhoods, of which 4432 showed evidence of differential abundance (figure 5D–F). Although CAFs significantly infiltrated into GCPM (figure 1E), the number of iCAFs was significantly decreased according to further differential analyses (CXCL14+iCAFs: p=2.1e−07). In contrast, the number of mCAFs significantly increased in GCPM (THBS2+mCAFs: p=1.9e−07; KRT8+mCAFs: p=7.6e−06) (figure 5F,G). These results illustrate the substantial compositional shift of CAFs in GCPM, with diminished iCAF components but excessive accumulation of mCAF components. Further mIF assays of FAP, αSMA and THBS2 verified the significant enrichment of THBS2+mCAFs in GCPM (figure 5H).

We further verified the levels of THBS2+mCAF marker genes in GCPM via in-house RNA-seq data. Paired analyses revealed that THBS2+mCAF marker genes were significantly more abundant in GCPM than in GC (*THBS2*: p=0.0001; *FAP*: p=0.001; *IGF1*: p=0.0001) (figure 5I). On the basis of TCGA database, we observed a significant prognostic disadvantage in patients with GC with a greater percentage of THBS2+CAFs (5-year OS: 51.3% vs 65.2%, p=0.007; 5-year PFS: 48.4% vs 62.8%, p=0.005) (figure 5J). In addition, a higher score for THBS2+-CAFs was related to unfavourable OS for patients with multiple cancers (online supplemental figure S7F).

We then attempted to identify cell lineages related to the efficacy of immunotherapy in GCPM (figure 5K–5O). Among the stromal components, THBS2+mCAFs were preferentially enriched in the ICB-resistant group (figure 5K,L). Among the genes expressed by CAFs in the GCPM tumour nest, DEG analyses between ICB-sensitive and ICB-resistant CAFs revealed that *THBS2*, *LUM*, *DCN* and *IGF1* were overexpressed in ICB-resistant CAFs (figure 5M,N), emphasising the role of THBS2+mCAFs in ICB resistance (figure 5O).

Taken together, the results revealed that the stromal components of GCPM distinctly differ from that of primary GC, with a significant enrichment of THBS2+mCAFs, which exhibited an enhanced protumoral phenotype and might be associated with ICB resistance in patients with GCPM.

THBS2+mCAFs secrete complement C3 to recruit TRM-derived TAMs to GCPM via the C3-C3AR1 axis

To analyse the phenotypic relationships of the various components in the TME of GCPM, we examined the correlations across all the cell lineages (figure 6A). We observed strong correlations between PCs and endothelial cells, between iCAFs and chief cells and between mCAFs and macrophages, suggesting the colocalisation of these components (figure 6A). Interestingly, there was a robust correlation between mCAFs and macrophages (R=0.48, p=2.8e−5) (figure 6B), indicating that there might be underlying interactions between these two important participants in the TME, thereby forming a stroma-myeloid niche.

We then used CellChat[34] to deduce the cell-cell interactions. Strong cell-cell interactions via complement C3-C3AR1 were observed between mCAFs and macrophages (figure 6C). Recently, non-classical functions of complement C3 exerted mainly through the cognate membrane-bound receptor C3a receptor 1 (C3AR1) have been reported.[35] We observed that the expression of *C3* was highest in mCAFs, whereas the expression of *C3AR1* was highest in macrophages (figure 6D,E). Subsequent mIF assays revealed robust colocalisation between C3 and FAP, verifying the capacity of CAFs to secrete complement component C3 (online supplemental figure S8A). In addition, mIF assays confirmed the expression of C3AR on macrophages (online supplemental figure S8B). These findings confirmed the strong cell-cell interaction between mCAFs and macrophages via the complement C3-C3AR1 axis.

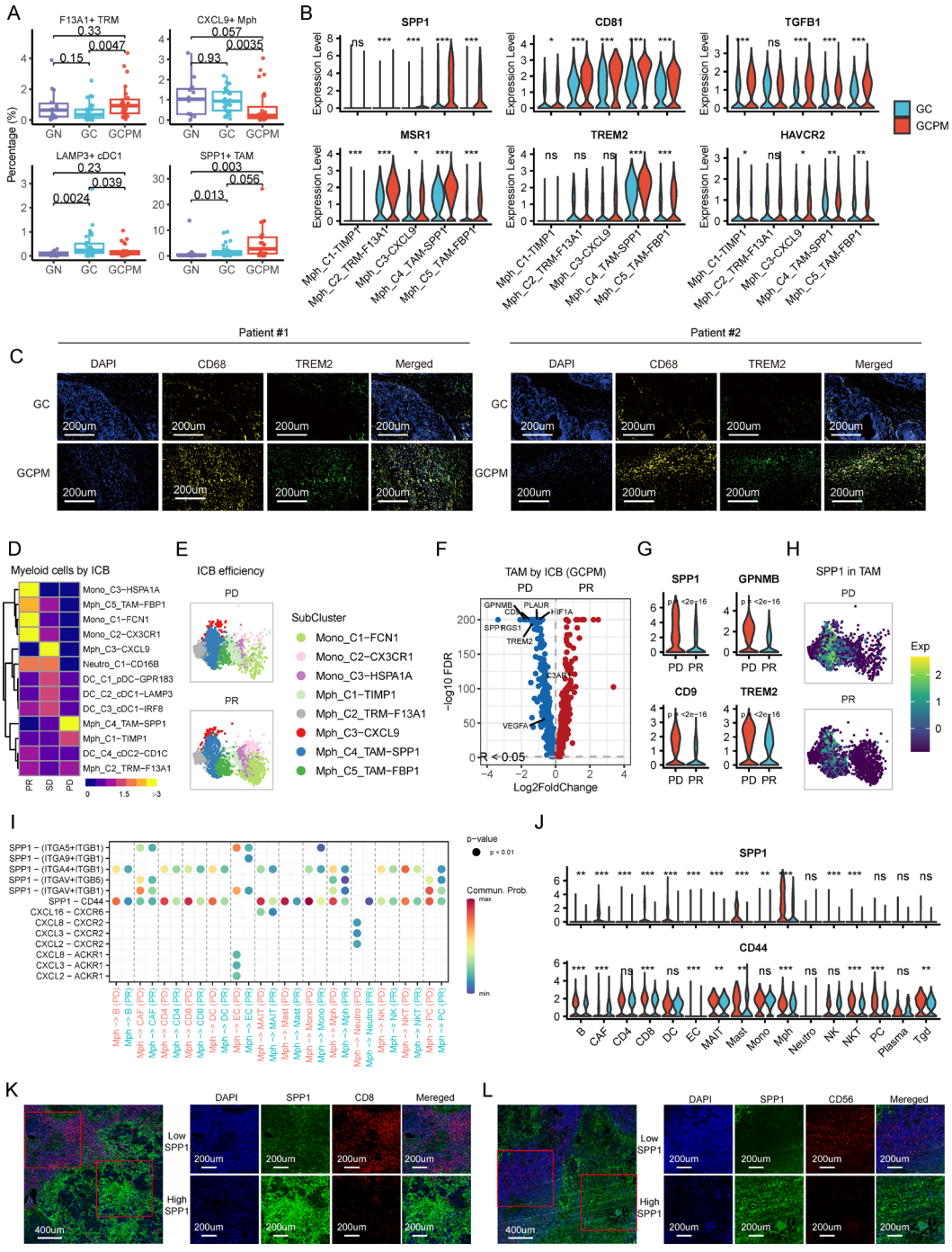

Figure 4 Relationship of tumour-associated macrophages with immunotherapy efficiency. (A) Box plot comparing the abundance of myeloid cell subclusters across gastric normal (GN) tissues (n=14), primary gastric cancer (GC) tissues (n=31) and gastric cancer peritoneal metastases (GCPM) tissues (n=24). The statistical significance was tested via Student's t-test. (B) Violin plot comparing the expression levels of *SPP1*, *CD81*, *TGFB1*, *MSR1*, *TREM2* and *HAVCR2* in the GCPM and GC samples. The statistical significance was tested via Wilcoxon test. (C) Multiplex immunofluorescence of DAPI, CD68 and TREM2 in GC and GCPM samples. The left and right panels are images of two representative patients. (D) Heatmap displaying the distribution of myeloid cells across different immunotherapy responses, including partial response (PR) (n=5), stable disease (SD) (n=4) and progressive disease (PD) (n=5), as estimated by Ro/e. (E) Uniform Manifold Approximation and Projection (UMAP) graph displaying the distribution of myeloid cells across different immunotherapy responses (PR vs PD). (F) Volcano plot showing the differentially expressed genes (DEGs) of monocytes/macrophages according to immunotherapy response (PR vs PD) in GCPMs. (G) Violin plot showing the expression of *SPP1*, *GPNMB*, *CD9* and *TREM2* in monocytes/macrophages according to immunotherapy response (PR vs PD) in GCPM. The statistical significance was tested via Wilcoxon test. (H) UMAP plot showing the expression of *SPP1* in monocytes/macrophages according to immunotherapy response (PR vs PD) in GCPM. (I) Dot plot showing the cell-cell interactions of macrophages with other cell types, comparing PRs and PDs. (J) Violin plot showing the expression of *SPP1* and *CD44* in all cell types according to immunotherapy response (PR vs PD) in GCPM. The statistical significance was tested via Wilcoxon test. (K) Multiplex immunofluorescence of DAPI, SPP1 and CD8 in GCPM. Top panel: low SPP1 level; bottom panel: high SPP1 level. (L) Multiplex immunofluorescence of DAPI, SPP1 and CD56 in GCPM. Top panel: low SPP1 level; bottom panel: high SPP1 level. Significance: ns, not significant; *p<0.05; **p<0.01; ***p<0.001. ICB, immune checkpoint blockade.

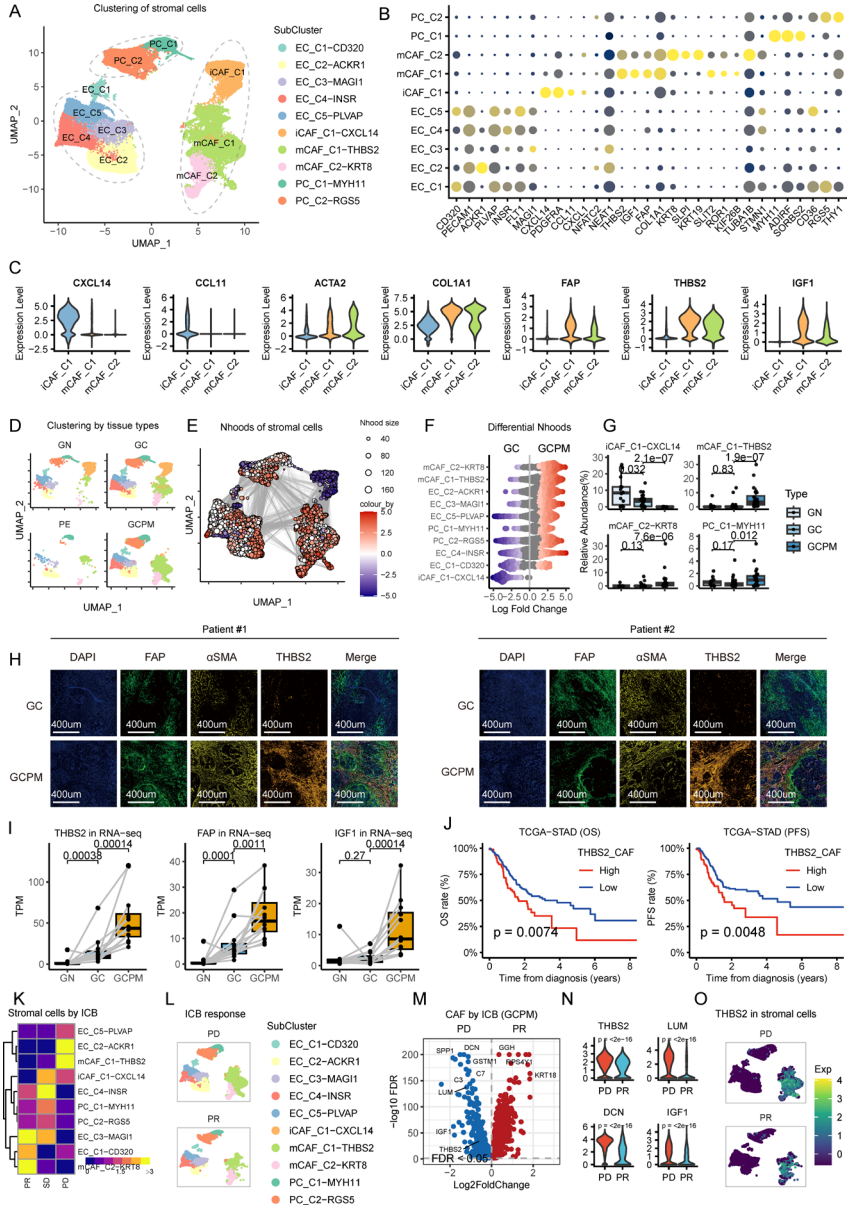

Figure 5 Landscape of stromal cells and relationship of stromal cells with immunotherapy efficiency. (A) Uniform Manifold Approximation and Projection (UMAP) embedding of 10 stromal cell subclusters, including 4 endothelial cell (EC) subclusters, 3 cancer-associated fibroblast (CAF) subclusters and 2 pericyte (PC) subclusters. (B) Dot plot showing the RNA expression of marker genes used to define the stromal cell types. (C) Violin plot showing the expression of *CXCL14*, *CCL11*, *ACTA2* (encoding αSMA), *COL1A1*, *FAP*, *THBS2* and *IGF1* according to stromal cell type. (D) UMAP embedding of single-cell RNA sequencing (scRNA-seq) data for gastric normal (GN) tissues, primary gastric cancer (GC) tissues, gastric cancer peritoneal metastases (GCPM) tissues and peritoneum (PE) tissues. (E) Graph representation of Nhoods identified by Milo in stromal cells. Nodes are Nhoods, coloured by their log2 fold change (FC) between GCPMs (n=24) and GCs (n=31). Non-differentially abundant neighbourhoods (false discovery rate ≥0.1) are coloured white, and sizes correspond to the number of cells in a neighbourhood. The graph edges depict the number of cells shared between adjacent Nhoods. (F) Beeswarm plot showing the distribution of adjusted log2 FC in abundance between GCPMs (n=24) and GCs (n=31) in Nhoods according to stromal cell type. (G) Box plot comparing the abundance of stromal cell subclusters across GNs (n=14), GCs (n=31) and GCPMs (n=24). The statistical significance was tested via the Wilcoxon test. (H) Multiplex immunofluorescence of DAPI, FAP, αSMA and THBS2 in the GC and GCPM samples. The left and right panels are images of two representative patients. (I) Box plot comparing the RNA expression of *THBS2*, *FAP* and *IGF1* in 12 pairs of matched GN, GC and GCPM samples. The statistical significance was tested via paired Wilcoxon test. (J) Overall survival (OS) and progression-free survival (PFS) in the TCGA-STAD cohort stratified by the number of THBS2+CAFs. The numbers of THBS2+CAFs were inferred via the single-sample gene set variation analysis (ssGSVA) method. The statistical significance was tested via log-rank test. (K) Heatmap displaying the distribution of stromal cells across different immunotherapy responses, including partial response (PR) (n=5), stable disease (SD) (n=4) and progressive disease (PD) (n=5), as estimated by Ro/e. (L) UMAP graph displaying the distribution of stromal cells across different immunotherapy response groups (PR vs PD). (M) Volcano plot showing the differentially expressed genes (DEGs) of CAFs according to immunotherapy response (PR vs PD) in GCPM. (N) Violin plot showing the expression of *THBS2*, *LUM*, *DCN* and *IGF1* in CAFs according to immunotherapy response (PR vs PD) in GCPM. The statistical significance was tested via Wilcoxon test. (O) UMAP plot showing the expression of *THBS2* in CAFs according to immunotherapy response (PR vs PD) in GCPM. αSMA, alpha smooth muscle actin; DAPI, 4',6-diamidino-2-phenylindole; FAP, fibroblast activation protein alpha; ICB, immune checkpoint blockade.

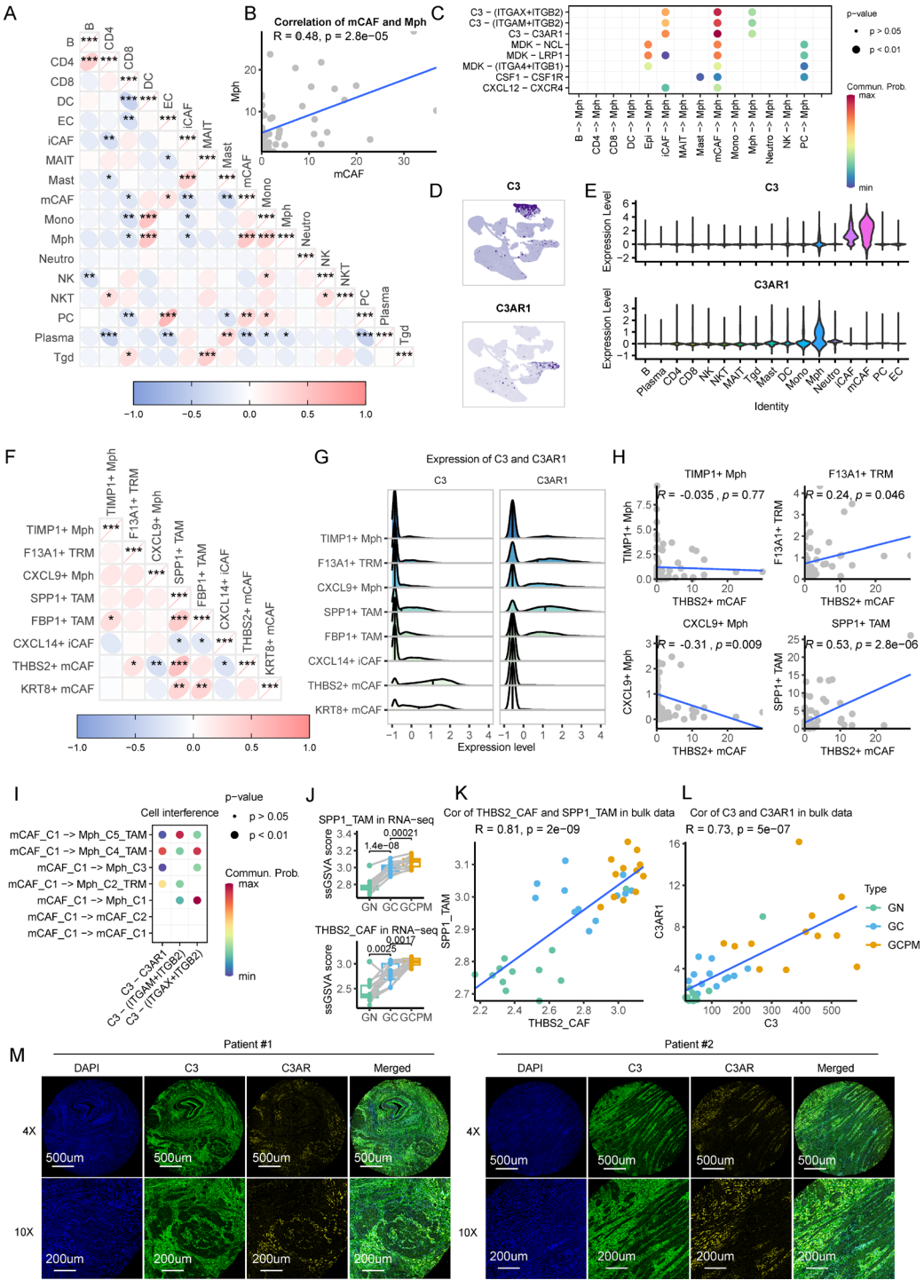

Figure 6 Crosstalk between fibroblasts and macrophages in peritoneal metastases of gastric cancer. (A) Heatmap displaying the correlations across all cell types in the single-cell data. Gastric normal (GN) tissues (n=14), primary gastric cancer (GC) tissues (n=31) and gastric cancer peritoneal metastases (GCPM) tissues (n=24) were included in the analyses. (B) Correlations between cancer-associated fibroblasts (CAFs) and macrophages in the single-cell data. (C) Dot plot showing the cell-cell interactions of all cell types on macrophages, comparing the GCPM and GC samples. (D) Uniform Manifold Approximation and Projection (UMAP) plot showing the expression of *C3* and *C3AR1* in all cell types. (E) Violin plot showing the expression of *C3* and *C3AR1* in all cell types. (F) Heatmap displaying the correlations between CAFs and macrophages in the single-cell data. (G) Rideline plot showing the expression of *C3* and *C3AR1* in CAFs and macrophages. (H) Correlations between THBS2+matrix CAFs (mCAFs) and macrophage subclusters in the single-cell data. (I) Dot plot showing the function of the C3-C3AR1 axis in THBS2+mCAFs in macrophage subclusters. (J) Box plot comparing the levels of SPP1+tumour-associated macrophages (TAMs) and THBS2+mCAFs in 12 pairs of matched GN, GC and GCPM samples. The statistical significance was tested via paired Student's t-test. (K) Correlations between SPP1+TAMs and THBS2+mCAFs in 12 pairs of matched GN, GC and GCPM RNA sequencing (RNA-seq) data. (L) Correlations between the expression of *C3* and *C3AR1* in 12 pairs of matched GN, GC and GCPM RNA-seq data. (M) Multiplex immunofluorescence of DAPI, C3 and C3AR1 to show the interaction of THBS2+mCAFs and SPP1+TAMs in GCPM. The left and right panels are images of two representative patients. Significance of correlation: *p<0.05; **p<0.01; ***p<0.001. DC, dendritic cell; EC, endothelial cell; NK, natural killer cell; NKT, natural killer T cell; PC, pericyte.

Correlation analyses revealed that THBS2+mCAFs were strongly correlated with SPP1+TAMs (R=0.53, p=2.8e−6), and were negatively related to CXCL9+Mph cells (R=−0.31, p=0.009) (figure 6F,H, online supplemental figure S8C and online supplemental figure S9A). The expression analyses revealed that complement *C3* was highly expressed on THBS2+mCAFs, whereas its receptor C3AR1 was highly expressed on SPP1+TAMs (figure 6G). Subsequent cell--cell interference analyses confirmed the interaction between THBS2+mCAFs and SPP1+TAMs via the C3-C3AR1 axis (figure 6I). The paired analyses of the bulk RNA-seq data verified that the number of SPP1+TAMs and THBS2+mCAFs increased simultaneously in the GCPM samples compared with the primary GC and GN samples (figure 6J), indicating a strong correlation (R=0.81, p=2e−9) (figure 6K,L and online supplemental figure S9B), highlighting the high prevalence of C3-C3AR1 interference in the tumour ecosystem. In addition, mIF assays observed that cells with C3AR presentation were attracted in regions with high C3 concentrations (figure 6M). As a consequence, SPP1+TAMs were significantly colocalised with THBS2+mCAFs, which has also been demonstrated by the robust colocalisation of C3 and C3AR1 (figure 6M), as well as another robust colocalisation of C3AR1 and SPP1 (online supplemental figure S10).

Taken together, multiple findings support the existence of a protumoral stroma-myeloid niche in GCPM. In this niche, THBS2+mCAFs release complement C3, which is associated with the recruitment and accumulation of SPP1+TAMs via C3AR1[35] (figure 6).

The stroma-myeloid niche of THBS2+mCAFs and SPP1+TAMs meditates immunotherapy resistance in GCPMs via the C3-C3AR1 axis

In the above analyses, we observed that the C3-C3AR1 axis of THBS2+mCAFs might facilitate the recruitment of F13A1+TRMs and contribute to the accumulation of SPP1+TAMs (figure 6). Next, we explored and validated the underlying role of the C3-C3AR1 axis in the immunotherapy resistance of GCPM. In 12 pairs of GN, GC and GCPM samples, the increase of C3 and its receptor C3AR1 was among the most significant changes observed across all cytokines (figure 7A). The scRNA-seq and bulk RNA-seq data suggested that *C3* and its receptor *C3AR1* increased markedly in the GCPM nests (figure 7B,C). The results from ELISA revealed that malignant ascites from patients with GC and other cancers contained greater concentration of C3 (GC: p=0.0016; other cancers: p=0.00035), whereas the C3 concentration in non-malignant ascites was the same as that in the peritoneal flushing fluid of non-ascites patients (figure 7D). Therefore, we observed and validated the aberrantly accumulated complement component C3 in GCPM, which might serve as a new marker or antitumoral target.

An in vitro migration assay revealed that the migration capacity of THP-1-derived macrophages and Raw264.7 macrophages was enhanced significantly even at a low concentration of C3 (5 ng/mL), and the migration capacity increased accordingly with increasing concentrations of C3 (figure 7E–H). Further mIF assays of GCPM revealed significant colocalisation of THBS2+mCAFs with TAMs (figure 7I) and exclusion of CD8+ T cells (figure 7J). Further cell-cell interaction analyses revealed that the crosstalk between THBS2+mCAFs and SPP1+TAMs via the C3-C3AR1 axis was related to immunotherapy resistance (figure 7K). The expression of both C3 and C3AR1 was significantly elevated in immunotherapy-resistant tumours (figure 7L), emphasising their roles in ICB resistance.

We next examined the therapeutic efficacy of SB290157, an antagonist of C3AR, in combination with an anti-PD1 antibody in a subcutaneous EO771 tumour model (figure 7M–O). We observed that EO771 tumours responded significantly to C3AR antagonist alone, and its combination with anti-PD1 antibody could significantly enhance the response to anti-PD1 antibody compared with anti-PD1 antibody alone (figure 7M,N and online supplemental figure S11A). Further mIF assays revealed that the C3AR antagonist could significantly restrain the expression of C3AR in TAMs, thereby eliminating TAMs and increasing the number of CD8+ T cells (figure 7O and online supplemental figure S11B,C).

In summary, in this study we comprehensively dissected the unique TME of GCPM, revealing that a stroma-myeloid crosstalk between THBS2+mCAFs and SPP1+TAMs via C3AR1 facilitates immunotherapy resistance. Thus, disrupting the C3-C3AR1 axis with a C3AR antagonist could remodel the tumour ecosystem and improve immunotherapy efficiency (figure 7P).

DISCUSSION

The high prevalence of peritoneal metastases represents a major obstacle in GC management. Therefore, a deeper understanding of GCPM is critical for understanding the complicated mechanisms driving the poor prognosis of patients with GCPM and for overcoming therapeutic resistance. In this study, we investigated the distinct and dynamic ecosystems of GCPM at single-cell resolution, deciphered the cellular and molecular alterations governing the TME of GCPM, and explored the underlying mechanisms related to the immunotherapy response of GCPM.

A key finding of this study was the unique TME of GCPM composed of stroma-myeloid niches, coordinating extensive protumoral and immunosuppressive functions, with excessive presentation of cytokines such as SPP1, TGFβ, IGF1, THBS2 and MMPs and membrane proteins such as TIM-3, TREM2 and MSR1. In this niche, SPP1+TAMs exceptionally infiltrate and play important roles in immunotherapy resistance, which have been reported to contribute greatly to the immunosuppressive TME,[22 29] with superior expression of *SPP1* and immune checkpoint proteins (*TIM-3*, *CD276* and *LGALS9*). Intriguingly, we also found that both antitumoral CXCL9+macrophages and protumoral SPP1+TAMs could be derived from TRMs. TRMs have been reported to be embryo-derived, long-lived and self-renewing and to have the potential ability to differentiate into functional M1/M2 macrophages.[36 37] Most TAMs in the TME are generated from TRMs, and we recently reported that TRMs also differentiate into antitumoral CXCL9+macrophages. However, the GCPM ecosystem orchestrates the transdifferentiation of TRMs and increases the infiltration of SPP1+TAMs. Overcoming the unbalanced differentiation of TRMs could reshape the TME and enhance antitumour immunity.

Most intriguingly, we observed that THBS2+mCAFs could release complement C3, crosstalk with TRM-derived SPP1+TAMs via C3-C3AR1 axis, and finally trigger the formation of the stroma-tumour niche.[38] Complement C3 has been shown to be elevated in multiple tumours and is associated with tumour immune evasion and therapy resistance.[39] However, the source of abnormally expressed complement remains largely unknown, which hinders further investigations into possible interventions. Recent studies revealed that multiple components in the TME have the capacity to release complement C3,

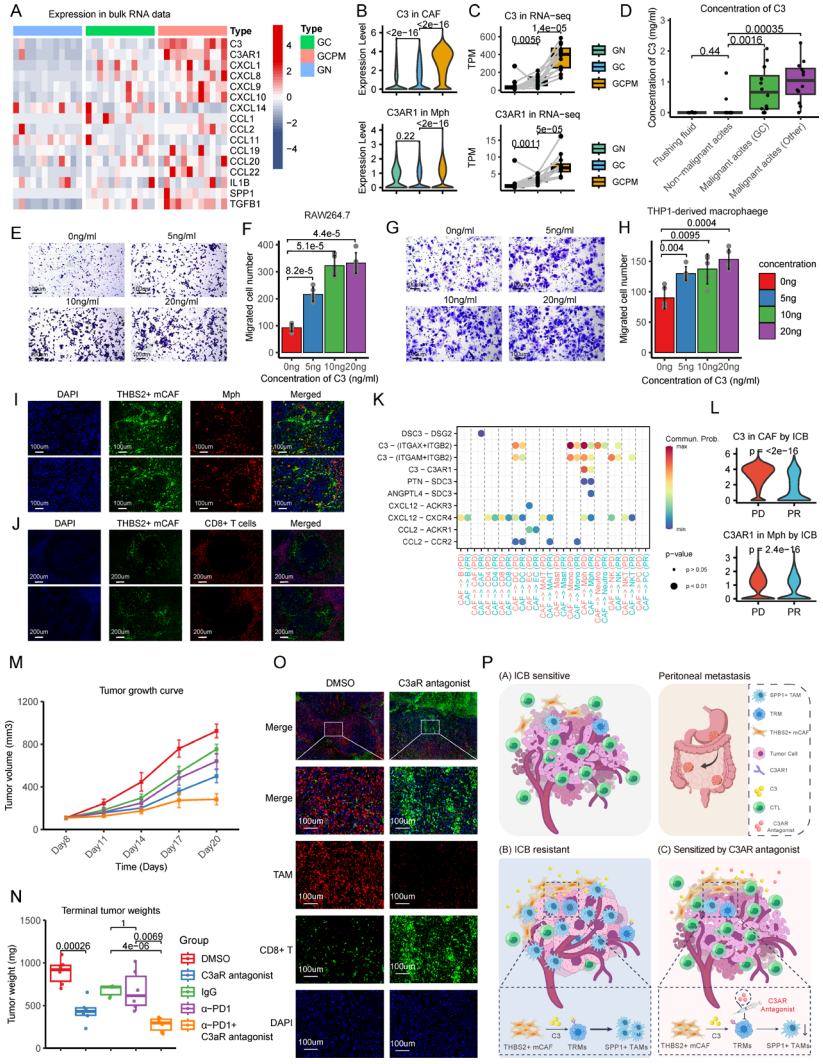

Figure 7 The crosstalk of fibroblasts and macrophages dominates the immunotherapy response in peritoneal metastases of gastric cancer. (A) Heatmap comparing the expression of cytokines in 12 pairs of matched gastric normal (GN), primary gastric cancer (GC) and gastric cancer peritoneal metastases (GCPM) samples. (B) Violin plot comparing the level of *C3* in cancer-associated fibroblasts (CAFs) and the level of *C3AR1* in macrophages in the single-cell RNA sequencing (scRNA-seq) data of GN, GC and GCPM samples. The statistical significance was tested via Wilcoxon test. (C) Box plot comparing the levels of *C3* and *C3AR1* in 12 pairs of matched GN, GC and GCPM samples. The statistical significance was tested via paired Wilcoxon test. (D) Box plot comparing the levels of C3 in the peritoneal flushing fluid of patients without ascites, the non-malignant ascites, the malignant ascites of patients with gastric cancer and the malignant ascites of patients with other cancers. The statistical significance was tested via Wilcoxon test. (E) Migration assay showing the capacity of RAW264.7 macrophages to migrate in response to different concentrations of C3 (stratified C3 concentrations: 0 ng/mL, 5 ng/mL, 10 ng/mL and 20 ng/mL). (F) Bar plot showing the number of migrated RAW264.7 macrophages as a function of the concentration of C3 (mean±SE). The statistical significance was tested via Student's t-test. (G) Migration assay showing the migratory capacity of THP-1-derived macrophages at different concentrations of C3 (stratified C3 concentrations: 0 ng/mL, 5 ng/mL, 10 ng/mL and 20 ng/mL). (H) Bar plot showing the number of migrated THP-1-derived macrophages according to the concentration of C3 (mean±SE). The statistical significance was tested via Student's t-test. (I) Multiplex immunofluorescence of DAPI, THBS2 and F4/80 to show the relationships between THBS2+matrix CAFs (mCAFs) and macrophages in GCPM. (J) Multiplex immunofluorescence of DAPI, THBS2 and CD8 to show the relationships between THBS2+mCAFs and CD8+ T cells in GCPM. (K) Dot plot showing the cell-cell interactions of macrophages with other cell types, comparing immune checkpoint blockade (ICB)-responsive and non-responsive samples. (L) Violin plot comparing the level of *C3* in CAFs and the level of *C3AR1* in macrophages in the scRNA-seq data of ICB-responsive and non-responsive samples. The statistical significance was tested via Wilcoxon test. (M–O) Subcutaneous tumour models of EO771 cells were constructed to evaluate the treatment efficacy of SB290157 (an antagonist of C3aR) and its combination with anti-PD1 antibody (α-PD1). Five groups were compared: dimethylsulfoxide (DMSO) (n=6), C3aR antagonist (n=6), IgG (n=6), α-PD1 (n=6), C3AR antagonist plus α-PD1 (n=6). (M) Growth curves of subcutaneous tumours derived from EO771 cells in different treatment groups. (N) Terminal tumour weights of subcutaneous tumours derived from EO771 cells in different treatment groups. The values are expressed as mean±SE. The statistical significance was tested via Student's t-test. (O) Multiplex immunofluorescence assays were used to explore the abundance of macrophages (F4/80) and CD8+ T cells (CD8) in subcutaneous tumours derived from EO771 cells in different treatment groups. (P) Proposed working model based on this study. The model shows that THBS2+mCAFs can release complement C3 to recruit tissue-resident macrophage-derived (TRM-derived) SPP1+tumour-associated macrophages (TAMs), retraining the antitumour immune response via the C3-C3AR1 axis. In ICB-resistant tumours, the extensive accumulation of THBS2+mCAFs and TRM-derived SPP1+TAMs facilitates immunotherapy resistance, and the blockade of the C3-C3AR1 axis might disrupt this process and enhance immunotherapy efficiency.

including stromal cells, endothelial cells and myeloid cells,[40 41] which play important role in modulating GC progression.[42] We found that THBS2+mCAFs are another major source of complement C3, which appear to be the source of immunosuppression and immunotherapy resistance in GCPM. This report provided an excellent example of how mCAFs (αSMA+/FAP+) influence the TME, which challenges the classical theory that only iCAFs (αSMA−/FAP+) can act as proinflammatory entities,[43] providing a novel interpretation for alterations in the TME. The C3-C3AR1 interaction and its functions in TAM recruitment and accumulation provide an interventional target for further drug discovery.

We identified KLRD1+NKT cells as the major effector cells that potentiate ICB therapies in patients with GCPM. NKT cells, which exhibited both NK cell and T cell characteristics,[44] are an important population of innate lymphocytes that play important roles in immune surveillance against infectious and tumour diseases.[45] Owing to the important role of NKT cells in immunosurveillance and antitumour immunity, NKT cell-based immunotherapy has been a great area of interest. Multiple strategies have been used to target cancer via NKT cell-based immunotherapeutic approaches, including exogenous α-galactosylceramide administration to activate NKT cells, adoptive transfer of activated NKT cells and CAR-NKT therapies.[46] Although reports regarding the functions of NKT cells in ICB therapies remain limited, the current studies have linked NKT cells with improved ICB responses.[47 48] Therefore, further investigations of the mechanisms of how NKT cells facilitate ICB efficiency are warranted. Besides, our finding of the abundant GCPM-specific NKT cells in peripheral blood also supports CAR-NKT-based immunotherapy as a promising strategy.

In summary, this single-cell transcriptomic profile of 410 612 single cells provides a systematic perspective of the noticeably shifted TME of GCPM. We found that the stroma-myeloid niche composed of SPP1+TAMs and THBS2+mCAFs is the major source of ICB resistance. Moreover, we observed aberrantly accumulated THBS2+mCAF components, which facilitate the accumulation of TRM-derived SPP1+TAMs via the C3-C3AR1 axis, forming a protumoral and immunosuppressive stroma-myeloid niche in GCPM. Blocking the C3-C3AR1 axis disrupts the stroma-myeloid crosstalk and thereby significantly improves the benefits of ICB in *in vivo* models. Our findings provide new insights into the specialised TME underlying the immunotherapy resistance of GCPM and practical targets for drug discovery to potentiate ICB therapy.

METHODS

See the online supplemental methods.

Contributors H-YL is the guarantor of this study. YL: formal analysis, resources, methodology, writing—original draft, writing—review and editing; YoZ: data curation, formal analysis, visualisation, writing—original draft, writing—review and editing; R-CN: data curation, formal analysis, resources, writing—original draft, writing—review and editing; JH: investigation, resources, writing—original draft, writing—review and editing; Q-NW: data curation, resources, writing—review and editing; ZZ: data curation, resources, writing—review and editing; KY: data curation, resources, writing—review and editing; SY: investigation, methodology, writing—review and editing; B-WZ: investigation, methodology, writing—review and editing; Y-QP: investigation, methodology, writing—review and editing; YX: investigation, writing—original draft, writing—review and editing; C-CL: data curation, visualisation, writing—review and editing; QZ: investigation, formal analysis, writing—review and editing; YaZ: investigation, visualisation, writing—review and editing; JC: data curation, visualisation, writing—review and editing; Z-LZ: investigation, writing—review and editing; WW: resources, writing—original draft, writing—review and editing; Z-XL: conceptualisation, data curation, funding acquisition, project administration, supervision, writing—original draft, writing—review and editing, validation; H-YL: conceptualisation, resources, investigation, funding acquisition, project administration, supervision, writing—original draft, writing—review and editing, validation; R-HX: conceptualisation, methodology, funding acquisition, project administration, supervision, writing—original draft, writing—review and editing, validation.

Funding This study was supported by the National Key R&D Programme of China (2021YFA1302100), the National Natural Science Foundation of China (92374114, 82273402, 82321003, 81930065, 82173128, 82103586 and 32370698), Guangdong Special Support Plan (2023TX07Y430), the Science and Technology Programme of Guangdong (2019B020227002), the Natural Science Foundation of Guangdong Province (2019A1515011109, 2024A1515012888 and 2014A030312015), the Guangdong Basic and Applied Basic Research Foundation (2022A1515012458 and 2023B1515040030), the Science and Technology Programme of Guangzhou (202002030208, 202206080011 and 202206080008), the CAMS Innovation Fund for Medical Sciences (CIFMS) (2019-I2M-5-036), the Cancer Innovative Research Programme of Sun Yat-sen University Cancer Center (CIRP-SYSUCC-0004), Young Talents Programme of Sun Yat-sen University Cancer Center (YTP-SYSUCC-0029), the Chih Kuang Scholarship for Outstanding Young Physician-Scientists of Sun Yat-sen University Cancer Center (CKS-SYSUCC-2024009) and the Postdoctoral Fellowship Programme of CPSF (GZB20240907).

Competing interests None declared.

Patient and public involvement Patients and/or the public were not involved in the design, or conduct, or reporting, or dissemination plans of this research.

Patient consent for publication Not applicable.

Ethics approval This study was approved by the Ethics Committee of Sun Yat-sen University Cancer Center (no. SL-B2022-241-02) andthe Animal Experiments Committee of the Sun Yat-sen University (no. L102012023100A). Participants gave informed consent to participate in the study before taking part.

Provenance and peer review Not commissioned; externally peer reviewed.

Data availability statement Data are available in a public, open access repository. Data are available on reasonable request. The sample information is listed in online supplemental table S1. The 10X genomics raw data of this study are deposited in the Genome Sequence Archive for Human database (ID: HRA009064; link: https://ngdc.cncb.ac.cn/gsa-human/browse/HRA009064). Additionally, the GEXSCOPE single-cell matrix data are deposited in the Mendeley repository (ID: jwkc5t6r55). Previously published scRNA-seq data that were reanalysed and integrated into this study are available in the Gene Expression Omnibus database under accession code GSE183904. All the data that support the findings of this study are available from the corresponding author on reasonable request.

ORCID iDs
Yuanfang Li http://orcid.org/0000-0003-1762-2634
Yongqiang Zheng http://orcid.org/0000-0003-3246-2800
Run-Cong Nie http://orcid.org/0000-0003-3595-6304
Shuqiang Yuan http://orcid.org/0000-0003-3661-5069
Ze-Xian Liu http://orcid.org/0000-0001-9698-0610
Rui-Hua Xu http://orcid.org/0000-0001-9657-4380

REFERENCES

1 Sung H, Ferlay J, Siegel RL, *et al*. Global Cancer Statistics 2020: GLOBOCAN Estimates of Incidence and Mortality Worldwide for 36 Cancers in 185 Countries. *CA Cancer J Clin* 2021;71:209–49.
2 GBD 2017 Stomach Cancer Collaborators. The global, regional, and national burden of stomach cancer in 195 countries, 1990-2017: a systematic analysis for the Global Burden of Disease study 2017. *Lancet Gastroenterol Hepatol* 2020;5:42–54.
3 Torre LA, Siegel RL, Ward EM, *et al*. Global Cancer Incidence and Mortality Rates and Trends--An Update. *Cancer Epidemiol Biomarkers Prev* 2016;25:16–27.
4 Ajani JA, D'Amico TA, Bentrem DJ, *et al*. Gastric Cancer, Version 2.2022, NCCN Clinical Practice Guidelines in Oncology. *J Natl Compr Canc Netw* 2022;20:167–92.

5 Yao X, Ajani JA, Song S. Molecular biology and immunology of gastric cancer peritoneal metastasis. *Transl Gastroenterol Hepatol* 2020;5:57.
6 Virgilio E, Giarnieri E, Giovagnoli MR, *et al*. Gastric Cancer Cells in Peritoneal Lavage Fluid: A Systematic Review Comparing Cytological with Molecular Detection for Diagnosis of Peritoneal Metastases and Prediction of Peritoneal Recurrences. *Anticancer Res* 2018;38:1255–62.
7 Kanda M, Kodera Y. Molecular mechanisms of peritoneal dissemination in gastric cancer. *World J Gastroenterol* 2016;22:6829–40.
8 Shiozaki H, Elimova E, Slack RS, *et al*. Prognosis of gastric adenocarcinoma patients with various burdens of peritoneal metastases. *J Surg Oncol* 2016;113:29–35.
9 Gamboa AC, Winer JH. Cytoreductive Surgery and Hyperthermic Intraperitoneal Chemotherapy for Gastric Cancer. *Cancers (Basel)* 2019;11:1662.
10 Manzanedo I, Pereira F, Serrano Á, *et al*. Review of management and treatment of peritoneal metastases from gastric cancer origin. *J Gastrointest Oncol* 2021;12:S20–9.
11 Chen C, Zhang F, Zhou N, *et al*. Efficacy and safety of immune checkpoint inhibitors in advanced gastric or gastroesophageal junction cancer: a systematic review and meta-analysis. *Oncoimmunology* 2019;8:e1581547.
12 Taieb J, Moehler M, Boku N, *et al*. Evolution of checkpoint inhibitors for the treatment of metastatic gastric cancers: Current status and future perspectives. *Cancer Treat Rev* 2018;66:104–13.
13 Bartley AN, Washington MK, Colasacco C, *et al*. HER2 Testing and Clinical Decision Making in Gastroesophageal Adenocarcinoma: Guideline From the College of American Pathologists. *Am Soc Clin Pathol, Am Soc Clin Oncol, J Clin Oncol* 2017;35:446–64.
14 Janjigian YY, Shitara K, Moehler M, *et al*. First-line nivolumab plus chemotherapy versus chemotherapy alone for advanced gastric, gastro-oesophageal junction, and oesophageal adenocarcinoma (CheckMate 649): a randomised, open-label, phase 3 trial. *Lancet* 2021;398:27–40.
15 Qiu M-Z, Oh D-Y, Kato K, *et al*. Tislelizumab plus chemotherapy versus placebo plus chemotherapy as first line treatment for advanced gastric or gastro-oesophageal junction adenocarcinoma: RATIONALE-305 randomised, double blind, phase 3 trial. *BMJ* 2024;385:e078876.
16 Mizrak Kaya D, Nogueras-González GM, Harada K, *et al*. Risk of peritoneal metastases in patients who had negative peritoneal staging and received therapy for localized gastric adenocarcinoma. *J Surg Oncol* 2018;117:678–84.
17 Zheng L, Qin S, Si W, *et al*. Pan-cancer single-cell landscape of tumor-infiltrating T cells. *Science* 2021;374:abe6474.
18 Patel AP, Tirosh I, Trombetta JJ, *et al*. Single-cell RNA-seq highlights intratumoral heterogeneity in primary glioblastoma. *Science* 2014;344:1396–401.
19 Hebbandi Nanjundappa R, Shao K, Krishnamurthy P, *et al*. Invariant natural killer T cells in autoimmune cholangiopathies: Mechanistic insights and therapeutic implications. *Autoimmun Rev* 2024;23:103485.
20 Huang Q, Wu X, Wang Z, *et al*. The primordial differentiation of tumor-specific memory $CD8^+$ T cells as bona fide responders to PD-1/PD-L1 blockade in draining lymph nodes. *Cell* 2022;185:4049–66.
21 Willemsen L, de Winther MP. Macrophage subsets in atherosclerosis as defined by single-cell technologies. *J Pathol* 2020;250:705–14.
22 Bill R, Wirapati P, Messemaker M, *et al*. *CXCL9:SPP1* macrophage polarity identifies a network of cellular programs that control human cancers. *Science* 2023;381:515–24.
23 Nakamura K, Smyth MJ. TREM2 marks tumor-associated macrophages. *Signal Transduct Target Ther* 2020;5:233.
24 Zhang L, Li Z, Skrzypczynska KM, *et al*. Single-Cell Analyses Inform Mechanisms of Myeloid-Targeted Therapies in Colon Cancer. *Cell* 2020;181:442–59.
25 Yan W, Liu X, Ma H, *et al*. Tim-3 fosters HCC development by enhancing TGF-β-mediated alternative activation of macrophages. *Gut* 2015;64:1593–604.
26 Cao J, Spielmann M, Qiu X, *et al*. The single-cell transcriptional landscape of mammalian organogenesis. *Nature New Biol* 2019;566:496–502.
27 Hirano R, Okamoto K, Shinke M, *et al*. Tissue-resident macrophages are major tumor-associated macrophage resources, contributing to early TNBC development, recurrence, and metastases. *Commun Biol* 2023;6:144.
28 Cheng S, Li Z, Gao R, *et al*. A pan-cancer single-cell transcriptional atlas of tumor infiltrating myeloid cells. *Cell* 2021;184:792–809.
29 Klement JD, Paschall AV, Redd PS, *et al*. An osteopontin/CD44 immune checkpoint controls CD8+ T cell activation and tumor immune evasion. *J Clin Invest* 2018;128:5549–60.
30 Wu SZ, Roden DL, Wang C, *et al*. Stromal cell diversity associated with immune evasion in human triple-negative breast cancer. *EMBO J* 2020;39:e104063.
31 Zhang S, Yang H, Xiang X, *et al*. THBS2 is Closely Related to the Poor Prognosis and Immune Cell Infiltration of Gastric Cancer. *Front Genet* 2022;13:803460.
32 Ireland L, Santos A, Ahmed MS, *et al*. Chemoresistance in Pancreatic Cancer Is Driven by Stroma-Derived Insulin-Like Growth Factors. *Cancer Res* 2016;76:6851–63.
33 Dann E, Henderson NC, Teichmann SA, *et al*. Differential abundance testing on single-cell data using k-nearest neighbor graphs. *Nat Biotechnol* 2022;40:245–53.
34 Jin S, Guerrero-Juarez CF, Zhang L, *et al*. Inference and analysis of cell-cell communication using CellChat. *Nat Commun* 2021;12:1088.
35 Shinjyo N, Kagaya W, Pekna M. Interaction Between the Complement System and Infectious Agents - A Potential Mechanistic Link to Neurodegeneration and Dementia. *Front Cell Neurosci* 2021;15:710390.
36 Davies LC, Jenkins SJ, Allen JE, *et al*. Tissue-resident macrophages. *Nat Immunol* 2013;14:986–95.
37 Mass E, Nimmerjahn F, Kierdorf K, *et al*. Tissue-specific macrophages: how they develop and choreograph tissue biology. *Nat Rev Immunol* 2023;23:563–79.
38 Dunkelberger JR, Song W-C. Complement and its role in innate and adaptive immune responses. *Cell Res* 2010;20:34–50.
39 Lawal B, Tseng S-H, Olugbodi JO, *et al*. Pan-Cancer Analysis of Immune Complement Signature C3/C5/C3AR1/C5AR1 in Association with Tumor Immune Evasion and Therapy Resistance. *Cancers (Basel)* 2021;13:4124.
40 Mathern DR, Heeger PS. Molecules Great and Small: The Complement System. *Clin J Am Soc Nephrol* 2015;10:1636–50.
41 Davidson S, Efremova M, Riedel A, *et al*. Single-Cell RNA Sequencing Reveals a Dynamic Stromal Niche That Supports Tumor Growth. *Cell Rep* 2020;31:107628.
42 Yuan K, Ye J, Liu Z, *et al*. Complement C3 overexpression activates JAK2/STAT3 pathway and correlates with gastric cancer progression. *J Exp Clin Cancer Res* 2020;39:9.
43 Cords L, Tietscher S, Anzeneder T, *et al*. Cancer-associated fibroblast classification in single-cell and spatial proteomics data. *Nat Commun* 2023;14:4294.
44 Lee MS, Webb TJ. Novel lipid antigens for NKT cells in cancer. *Front Immunol* 2023;14:1173375.
45 Godfrey DI, Le Nours J, Andrews DM, *et al*. Unconventional T Cell Targets for Cancer Immunotherapy. *Immunity* 2018;48:453–73.
46 The Cancer Genome Atlas Research Network. Comprehensive molecular characterization of gastric adenocarcinoma. *Nature New Biol* 2014;513:202–9.
47 Hakanen HHE, Hernberg M, Mäkelä S, *et al*. Abstract A130: Metastatic melanoma patients responding to PD1 therapy have higher proportion of peripheral blood NKT-cells. *Cancer Immunol Res* 2019;7:A130.
48 Pilones KA, Kawashima N, Yang AM, *et al*. Invariant natural killer T cells regulate breast cancer response to radiation and CTLA-4 blockade. *Clin Cancer Res* 2009;15:597–606.
49 Luo H. Data from: single-cell transcriptome profiling elucidates the cellular determinants of immunotherapy response in gastric cancer peritoneal metastasis. Genome Sequence Archive for Human; 2024. Available: https://ngdc.cncb.ac.cn/gsa-human/browse/HRA009064
50 Kumar V, Ramnarayanan K, Sundar R, *et al*. Data from: single-cell atlas of lineage states, tumor microenvironment, and subtype-specific expression programs in gastric cancer [Gene Expression Omnibus]. 2023. Available: https://www.ncbi.nlm.nih.gov/geo/query/acc.cgi?acc=GSE183904